Plasmonically induced transparency in phase-coupled graphene nanoribbons

Shengxuan Xia,* Xiang Zhai, Lingling Wang, Yuanjiang Xiang, and Shuangchun Wen
Key Laboratory for Micro/Nano Optoelectronic Devices of Ministry of Education & Hunan Provincial Key Laboratory of Low-Dimensional Structural Physics and Devices, School of Physics and Electronics, Hunan University, Changsha 410082, China

(Received 8 February 2022; revised 3 June 2022; accepted 21 July 2022; published 2 August 2022)

Due to its transparent and highly dispersive nature, plasmonically induced transparency (PIT) has become an attractive field in the on-chip control of light. Conventional methods to achieve PIT are only limited to the lowest dipole-dipole or dipole-combined quadrupole modes by breaking structural symmetry. Consequently, a general methodological framework for accurately designing all-order PIT remains absent. In this paper, we propose a theoretical scheme to achieve unidirectional odd-to-even order PIT by establishing a model with two layers of periodic graphene nanoribbons. The underlying physical principles are uncovered by defining the additional resonant phase of one mode over the other as phase difference, which predicts that the PIT effects appear (disappear) generally near the positions where the phase difference is around odd (even) multiple numbers of π. Full-wave simulations and theoretical analysis are used to demonstrate our proposal, revealing that the proposed PIT concept possesses good robustness against both the ribbon width and the relative ribbon positions. Our results serve to provide an effective method to realize all-order PIT and to design PIT-based photonic devices.

DOI: 10.1103/PhysRevB.106.075401

I. INTRODUCTION

Surface plasmons, the collective oscillations of free electrons in the surface of conducting media, can concentrate the incident electromagnetic energy into extremely subwavelength scales [1,2]. This extraordinary property has gained multifield research interest from physics [3], chemistry [4], and biology [5] and has been reported to have various applications such as optical modulators [3,6], nanolasers [7], chemical reaction [4], sensors [8,9], and particle manipulation [10,11]. Additionally, the physical mechanism of surface plasmons provides a fruitful platform to achieve some classical phenomena, for example, the classical analogue of electromagnetically induced transparency [12,13], which is also known as plasmonically induced transparency (PIT) [12,14,15].

PIT is an effect driven by the interference between two excitation pathways in two coupled resonators [16,17]. If a plasmon mode can strongly (weakly or not) couple to incident light at some excitation conditions, it can work as a bright (dark) mode [12]. Bright plasmon modes are radiative, which means they are easy to be excited and measured with far-field plane-wave optical techniques and, therefore, are extensively studied [18]. Meanwhile, dark plasmon modes are nonradiative, which makes them difficult to be excited and measured with far-field techniques [19], but they can usually be generated through near-field couplings [20–22]. Note that both the bright and dark modes can be switched to each other in some cases, depending on the polarization condition [23]. When the bright and dark modes approach each other in both the resonant frequency and the real space, their destructive interferences will create a transparency window at the wavelength near the original bright mode in the optical spectrum [12,13,24]. Because of the ability to slow the light near the transparency window and strongly localize the electromagnetic field [25,26], PIT has great potential applications in the field of integrated photonic devices [27,28].

Recently, tremendous attention has been attracted to study the PIT effect in many types of resonators, such as in periodic metasurfaces/metamaterials and waveguide systems, which are either constructed by traditional metals (like Au and Ag) [12,14,29,30] and two-dimensional (2D) materials (such as graphene and black phosphorus) [23,31] or their combinations [32,33]. Among them, the more commonly proposed designs are constructed by nanostructure arrays [12,13,25,32,34]. The main features of this kind of system are that the PIT effects can be generally conserved if the symmetry of the system is broken [12,13,28,34–37], and it can be found that these systems mainly support the lowest order dipole-dipole mode coupled PIT effects [13,28,34,37]. Conversely, these features arouse two longstanding questions: Why can PIT effects be achieved by breaking the geometrical symmetry? Is the symmetry breaking a general method to achieve all-order PIT? These issues have severely hampered the design and application of PIT devices. Therefore, a general theoretical model that can quantitatively characterize all-order PIT is certainly important and highly desired.

To answer these questions and further reveal the physical controlling mechanisms behind them, in this paper, a parameter called *phase difference* is introduced to predict the existence of PIT. In terms of the plasmon wave functions (PWFs) within the classical electrostatic limit, we theoretically propose and numerically demonstrate how this parameter is related to the relative geometrical position of the coupled resonators and how it further tunes the PIT properties through a general rule by making use of the bright and dark

*Corresponding author: shengxuanxia@hnu.edu.cn

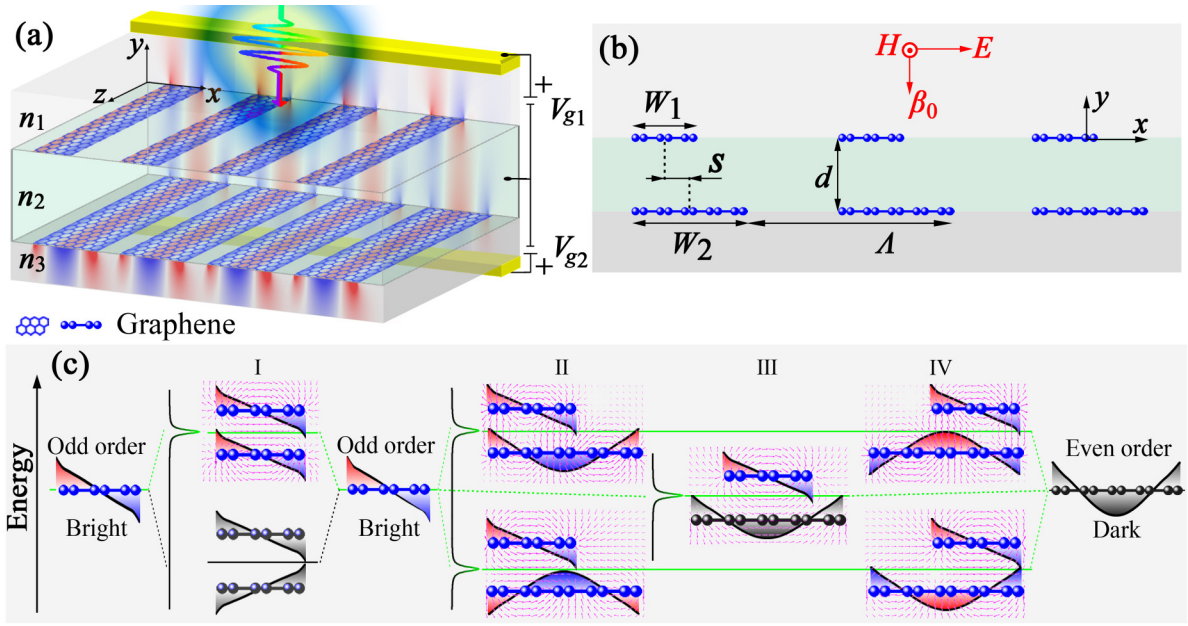

FIG. 1. (a) Three-dimensional (3D) and (b) two-dimensional (2D) geometrical diagrams of the proposed plasmonically induced transparency (PIT) device. Two graphene nanoribbon (GNR) layers are sandwiched among three dielectric layers that have refractive indexes of $n_1 = 1$, $n_2 = 1.5$, and $n_3 = 1.5$, respectively. The two ribbon layers are assumed to be with widths W_1 and W_2, distance d (60 nm), period Λ (1000 nm), and central-to-central shift s. A plane wave is incident from the positive y direction with the polarization direction perpendicular to the ribbon width. (c) Schematic representations of the energy-level diagram describing the plasmon couplings for different ribbon configurations. The two nanoribbons are uncoupled (cases I and III), asymmetrically coupled (upper plots in cases II and IV, antisymmetric mode), and symmetrically coupled (lower plots in cases II and IV, symmetric mode) when they are with same width (case I) or centrosymmetric (case III) and edge-aligned (cases II and IV) constructions, respectively.

modes in a model composed of two coupled periodic graphene nanoribbons (GNRs).

To this end, the structure of this paper is constructed as follows: In Sec. II A, we present the structure and materials under study and the energy-level schematic diagram of the proposed PIT effects. In Sec. II B, we briefly discuss the bright and dark modes supported by a single graphene ribbon layer. In Sec. II C, we study the existence, mechanism, and properties of the PIT effects in detail and demonstrate their relationships with coupling strengths and phase differences for different ribbon configurations. Then in Secs. II D and II E, we briefly discuss the robustness of ribbon width and sensing performance of the proposed PIT effect. Finally, we respectively summarize our findings in the conclusion section and present detailed theoretical calculations of PWFs in the appendixes.

II. RESULTS AND DISCUSSIONS

A. Model and materials

The analytical model under study is presented in Fig. 1. Two layers of periodic GNRs with different widths are stacked with central-to-central in-plane shift s and spaced by a distance d. A plane wave with the electric field polarized along the x direction is incident from the positive y direction. Here and in what follows, we only consider the case with normal incidence, unless specified otherwise. The three dielectric layers separated by the two graphene layers are assumed to be respectively dominated with refractive indexes of $n_1 = 1$, $n_2 = 1.5$, and $n_3 = 1.5$, so that we can elucidate the fundamental principles of PIT without loss of generality. From the practical point of view, these materials can be trivially extended to conductive media such as Si, SiO_2, or ion-gel since the silicon substrate with a proper doping level or the ion-gel can act as gate electrodes, and the voltage can be applied between the substrate and a metallic electrode on the graphene layer to dynamically tune graphene conductivity [38,39]. All the geometrical parameters are predefined, as shown in Figs. 1(a) and 1(b). The proposed structures are simulated by using finite-difference time-domain (FDTD) methods with Lumerical FDTD solutions. In both our theoretical and numerical calculations, we model the graphene sheet as a 2D surface characterized by an infinitesimally thin, local, and in-plane isotropic electrical conductivity $\sigma(\omega)$, which is expressed in terms of interband and intraband contributions and is widely used to model the optical property of graphene in both theoretical and experimental works [40–42]. Full details on this model and the parameters can be found in Refs. [23,43,44]. Notably, the Fermi level of graphene is assumed to be 0.6 eV in this paper, which is a conservative value within experimentally feasibly ones reached by electrostatic gates [45,46]. We also note that our proposals are general, and our fundamental conclusions do not depend on the choice of the Fermi level of graphene or other dielectric parameters if the choices can guarantee efficient excitation of the plasmons.

B. PWFs in single-layer GNR

The proposed PIT effects are the results of strong coupling between two ribbon layers; how the fundamental plasmon

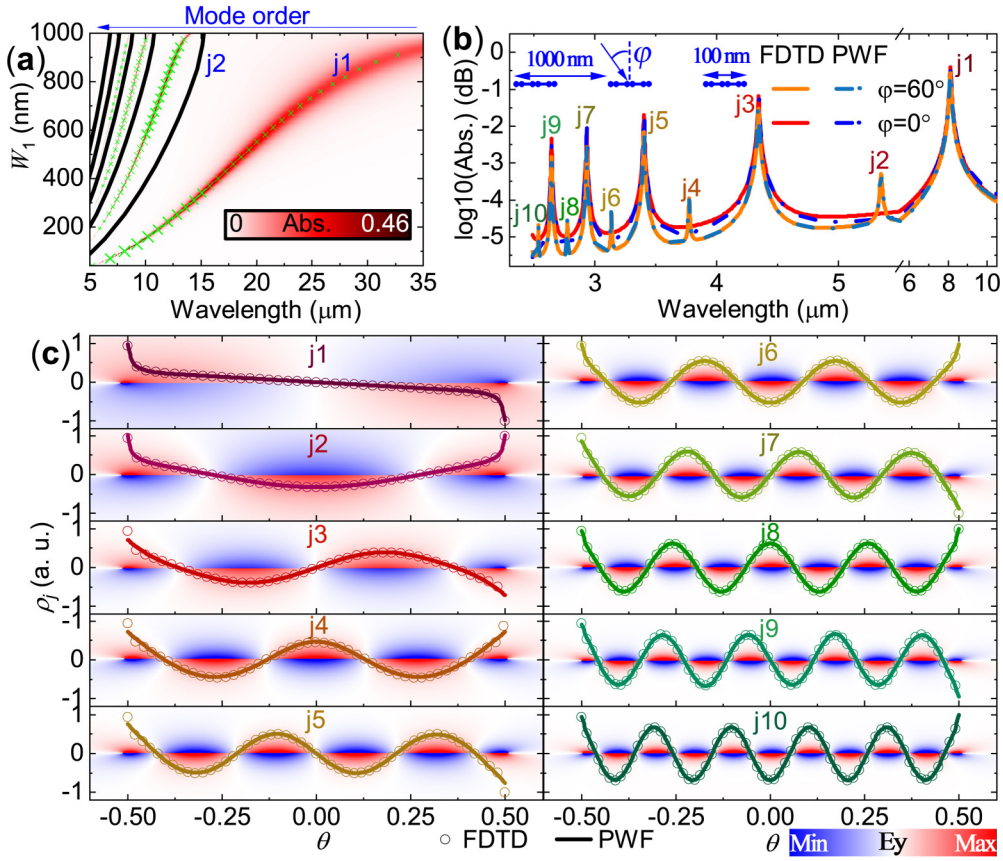

FIG. 2. Plasmon response of single-layer periodic graphene nanoribbons (GNRs). (a) Absorption map for different ribbon widths. The cyan-colored crosses present the mode position from plasmon wave functions (PWFs), with their sizes proportional to the absorption maxima. The black lines plot the wavelength of the even-order dark modes that are captured by using oblique incidence. (b) Logarithmic scale absorption lines with $W_1 = 100$ nm and $\Lambda = 1000$ nm under normal and oblique incidence. The insert depicts the schematic diagram of the structure under oblique incidence. (c) Mode profiles of the first 10 lowest-order plasmon modes. The circles are the results of the finite-difference time domain (FDTD), while the lines are fitted by extracting the PWFs from the polarizability calculated with FDTD.

modes behave in each ribbon layer will determine how they interact with each other. Therefore, it is essential to start by analyzing the fundamental plasmon modes in only one-layer GNR. Figure 2 presents some fundamental properties of the first 10 lowest-order plasmon modes. Firstly, it is shown in Fig. 2(a) that the strong absorptions exist in the absorption map that reveals the excitation of the plasmons, but these plasmons are all odd-order modes. With the increase of the ribbon width, their resonant wavelengths shift to longer wavelengths. This is because the multimode plasmon resonances can be viewed as Fabry-Pérot cavity modes that travel along the ribbon width and get reflected at the edge terminal [47,48]; thus, the termination of the GNR acts both as a scattering source and as a reflection mirror. When the round-trip travel accumulates a $2j\pi$ phase (where j presents the mode order), it forms standing wave resonance so that the local electromagnetic field is trapped within the ribbon [49,50], as is clearly shown in Figs. 2(c) and S3(b) in the Supplemental Material [44]. The remarkable signature of these standing waves is that the jth-order mode has j nodes along the ribbon width, as shown in Figs. 2(c) and S3(b) in the Supplemental Material [44] and well predicted by the PWF. Therefore, the wider ribbon width will cost a longer trip to accumulate the resonant phase at each mode, resulting in longer wavelengths.

The other significant feature is that the even-order modes are not (weakly) excited under normal (oblique) incidence. To clearly illustrate this, we plot the numerically and theoretically calculated absorption spectra for the cases with two specified incident angles of 0° and 60°, respectively, as shown in Fig. 2(b) (evidence of odd-order plasmon excitations can be found in Fig. S3(b) in the Supplemental Material [44]). In addition to the good agreement between the results of the two methods, one can easily find that the even-order modes are completely dark under normal incidence. Their excitation efficiencies are almost two orders of magnitude smaller than those of the odd-order modes even at the oblique incident angle of 60°. The difference in excitation efficiency between the odd- and even-order modes is caused by the mode symmetry [19]. As the first 10 lowest-order eigenmode profiles shown in Fig. 2(c), all odd-/even-order modes have an asymmetric/symmetric field distribution. Considering that the mode moment is defined as $\zeta_j = \int d\theta \rho_j(\theta)\theta$ with $\theta = x/W$ being a dimensionless coordinate [see Eq. (A15) in Appendix A], the odd-/even-order modes have nonzero/zero mode moment and, thus, the high/low mode excitation efficiency (according to our calculation, the mode moment ζ_j of the odd mode is at least three orders bigger than that of the even order mode). Therefore, they can/cannot be observed in simulations or

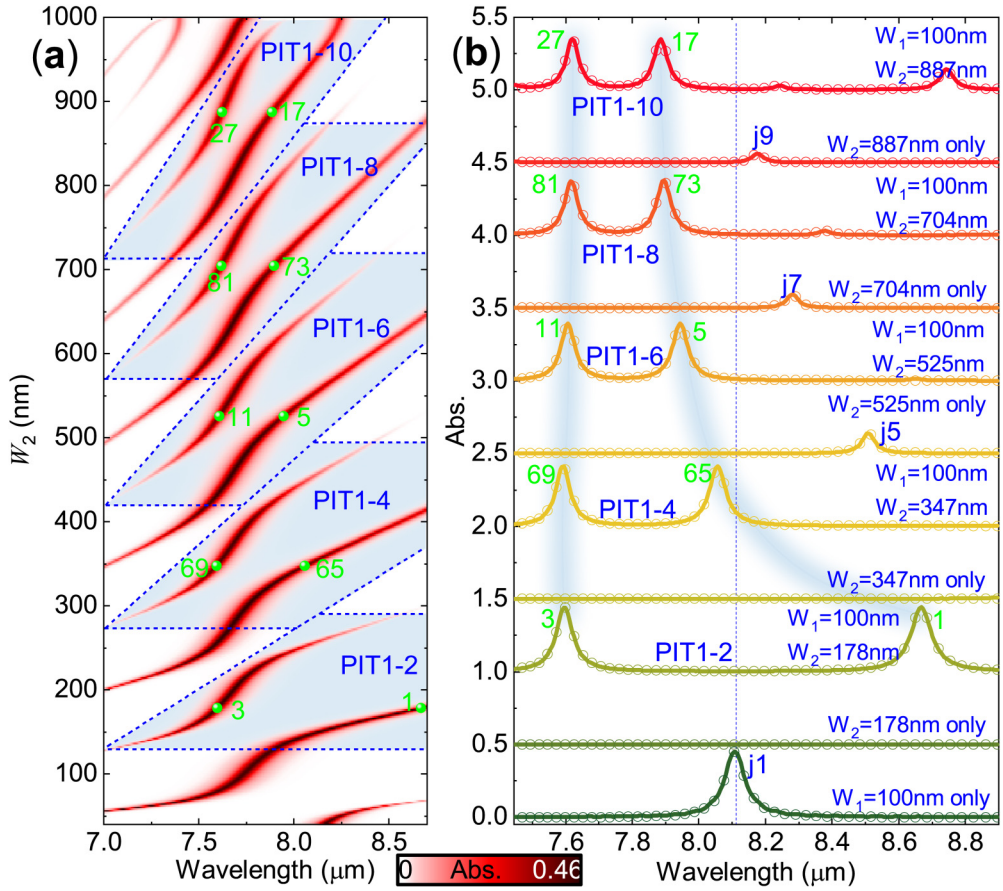

FIG. 3. (a) Calculated absorption map with sweeping wavelength and ribbon width of the second ribbon layer, where we have $W_1 = 100$ nm and $s = -|W_2 - W_1|/2$. (b) Linecuts of the absorption spectra for selected ribbon widths and different ribbon configurations. The two light-blue lines are guides for the eye. The identified numbers at the absorption maxima are in accordance with these positions shown in Fig. 4, which refer to the resonant positions of the symmetric mode (SM; smaller numbers) and asymmetric mode (AM; bigger numbers). Circles and lines correspond to the data from the finite-difference time domain (FDTD) and plasmon wave functions (PWFs), respectively.

experiments since they can/cannot be excited using standard plane-wave incidence configurations [51–53].

C. PIT in two layers of GNRs

In this part, we discuss our concept of achieving PIT effects by making full use of the features of the odd- and even-order modes. Odd-/even-order modes have nonzero/zero net mode moments and can strongly/weakly couple with incident light; therefore, they can play the role of bright/dark mode [12]. Considering that the wider ribbon width supports an increasing number of plasmon modes with increasing wavelength (see Figs. 2(a) and S1(a) in the Supplemental Material [44]), it is possible to construct a PIT device by using this primary property. To find this out, we carry out the simulations and display the results in Fig. 3(a) for the construction shown in Fig. 1 with $s = -|W_2 - W_1|/2$ (and also with $s = 0$, see Fig. S1(b) in the Supplemental Material [44]) for various ribbon widths of the second ribbon layer while fixing that of the first ribbon layer. The results clearly show that, compared with the case with only the first ribbon layer where only one peak is identified in the interested wavelength range, the edge-aligned ribbon layers produce two new distinct absorption peaks (also see Fig. S1 in the Supplemental Material [44]). They appear and fade away gradually with the increase of the ribbon width.

To gain physical insight into the nature of these peaks and distinguish whether they are the result of PIT, we firstly capture the absorption lines with two comparable absorption maxima and illustrate them in Fig. 3(b) (also see Fig. S3 in the Supplemental Material [44] for full wavelength range). These spectra indicate that the new emerging peaks locate at the positions between two odd-order modes of the second ribbon layer. For example, as shown in Fig. S3 in the Supplemental Material [44], peaks 1 and 3 appear within the range between the modes $j1$ and $j3$ of the case with $W_2 = 178$ nm only. One may find that these peaks (except for the case with $W_2 = 178$ nm) exhibit pronounced blueshift once compared with only the first ribbon layer, as the dashed line shows in Fig. 3(b). The blueshift of the high-order PIT can be explained by considering the change of the effective propagation constant that is caused by the existence and the coupling effect of the second graphene layer. This is because the existence of the second graphene layer not only brings the dielectric change but also leads the difference of the effective propagation constant between the symmetric mode (SM) and asymmetric mode (AM) that further shifts the resonant wavelengths (see Sec. S5 in the Supplemental Material

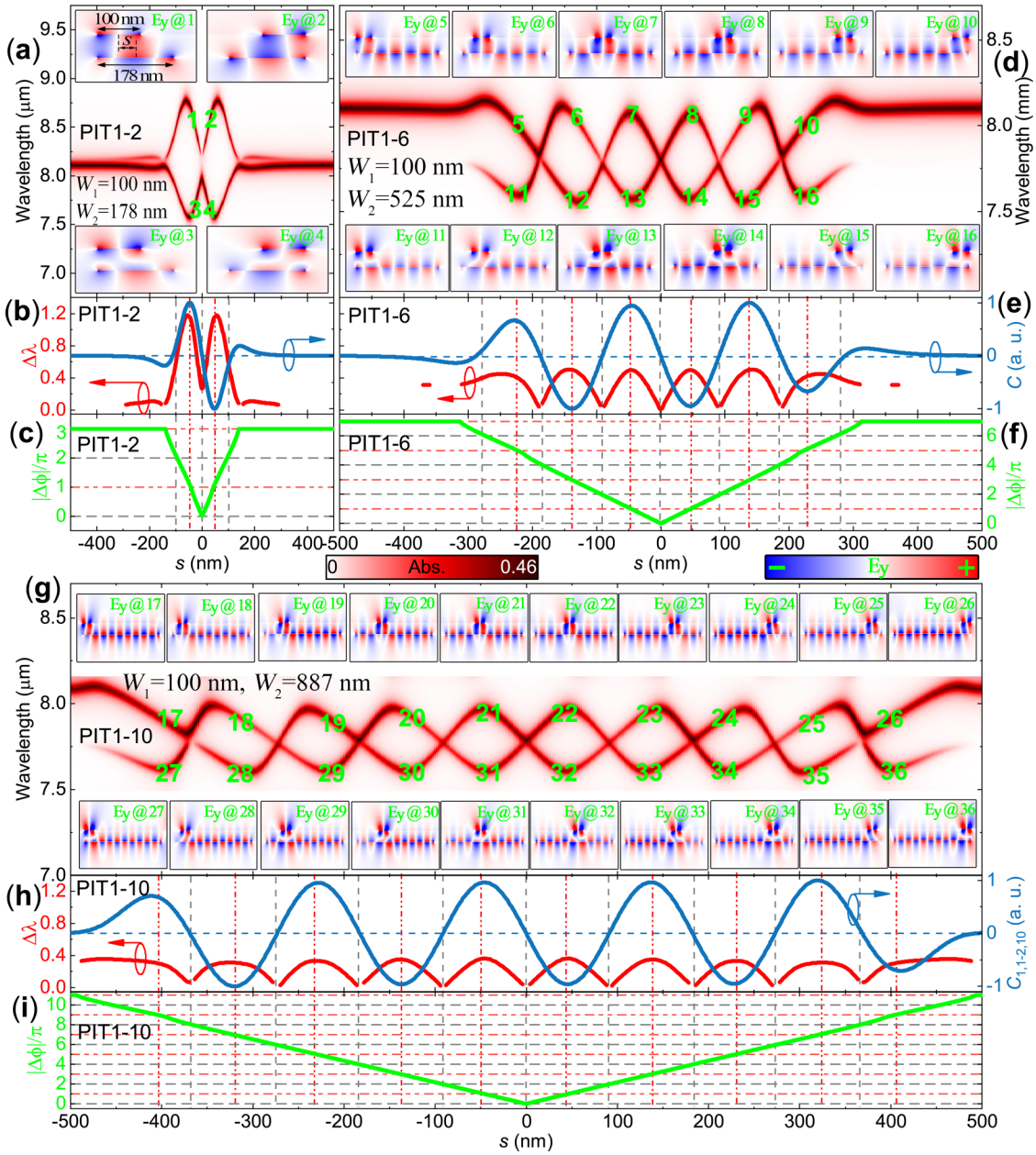

FIG. 4. Absorption maps for the (a) plasmonically induced transparency (PIT)1-2, (d) PIT1-6, and (g) PIT1-10 effects with different ribbon shift s. The inserts are the field distributions corresponding to the positions labeled by the cyan-colored numbers. (b), (e), and (h) PIT window width (left axis), coupling strength (right axis), and (c), (f), and (i) corresponding phase differences of (a)–(c) PIT1-2, (d)–(f) PIT1-6, and (g)–(i) PIT1-10 for different ribbon shift s, respectively.

[44] for more discussion). Notably, this blueshift is observed only when the coupling distance between the bright and dark modes is fixed. For the parameters used in this paper, the PIT effects can be maintained if the effective coupling distance is $<$150 nm (see Sec. S4 in the Supplemental Material [44] for details).

In addition, further examining the resonant field at these peaks, one can find the nature of these localized surface plasmons. As shown in Fig. 4 (also see Fig. S4 in the Supplemental Material [44]) by the inserts labeled with the corresponding numbers, the upper layer bright mode always keeps a dipole mode resonance, while the lower dark resonator is featured by an even-ordered mode with continuously increasing mode order j. The mode at the longer wavelength corresponds to an in-phase charge distribution where the charge carriers of the same sign are induced in the lower ribbon layer, which is named SM for convenience. In contrast, the mode at a shorter wavelength is excited when out-of-phase charge carriers are induced, which we call AM. The attraction between the asymmetric and symmetric charge carrier distributions in the second ribbon layer leads to an increase in restoring force and thus to a shift in the energy of the AM to higher energies compared with the SM. Therefore, the features of absorption lines and the near-field distributions reveal the fact that these peaks are indeed the results of different ordered PIT [12,13,23,54]. For conceptual discussion, the PIT

effect that is induced by the bth-order bright mode and the dth-order dark mode is abbreviated as PITb-d. Accordingly, we observe all-order PIT effects that are induced by the couplings from the first odd-order bright mode to the even-order dark mode from the lowest PIT1-2 to the highest PIT1-10 for the fixed period of 1 μm. Note that the highest 10th-order plasmon mode is used so that we can demonstrate the high efficiency of our proposal in inducing PIT and draw our conclusion for different mode orders without loss of generality. In all cases, the agreements between the analytical results obtained with PWFs [as plotted with lines in Fig. 3(b)] and the numerical results (represented with dots) are nearly perfect.

To understand the physical origin of these newly emerging PIT effects as well as the mechanisms controlling them, we present extensive numerical simulations and PWF-based theoretical analyses on different ribbon positions that allow us to fully characterize the dependence of the PIT spectra on their relative geometrical parameters. Figure 4 illustrates the absorption maps of three selected PIT effects for different ribbon shift s within one period (see Fig. S4 in the Supplemental Material [44] for other ordered PIT). One can find that the PIT window reappears and disappears with the change of their relative position, which is also revealed by tracking the wavelength difference of the absorption maxima, as shown in the left axes of Figs. 4(b), 4(e), and 4(h).

The underlying physics involved in the characteristics of these PIT effects can be quantitatively analyzed by putting additional insights into the phase difference and the related coupling strength. With the help of the PWF (see Appendixes), we plot the coupling strength (to the second-nearest neighbor, see Eq. (B6) in Appendix B and Sec. S7 in the Supplemental Material [44]) as well as the phase difference (see Appendix D for details about its definition and calculation) between the two coupled modes of the ribbon layers in the right axes of Figs. 4(b), 4(e), and 4(h) and in Figs. 4(c), 4(f), and 4(i), respectively. The PIT effects take place near the positions where the coupling strength obtains its maximum, and more notably, the phase difference is around odd multiple numbers of π, whereas the PIT windows disappear at the places where the coupling strength takes its minimum and the phase difference approaches even multiple numbers of π. However, one may find that, for the cases with relatively low-order dark modes (that is from PIT1-2 to PIT1-8), the PIT effects disappear when s approaches the boundary of each unit even if the phase difference is an odd multiple number of π; this is because there is no vertically overlapped region and, therefore, the interaction between the two ribbon layers is weak, as shown in the right axes of Figs. 4(b), 4(e), and 4(h) (also see Figs. S4(b) and S4(e) in the Supplemental Material [44]).

In addition to the existence of these PITs, the number of transparency windows is under the control of the phase difference. It is shown in Fig. 2 that the plasmon mode with order j has a resonant phase $j\pi$ for a single trip along the ribbon surface. As a result, the total resonant phase of the bth-order bright mode and the dth-order dark mode is $(b+d)\pi$. Considering two facts, firstly, to make sure of the existence of the PIT effect, the two ribbons must have an overlapped region to guarantee a strong coupling between the two modes which, according to our calculation, can be further guaranteed by a minimum π phase resonance in each ribbon within this overlapped region (e.g., as can be seen from the inserts in Fig. 4 that the resonant phase within the overlapped region is π—the single trip resonant phase of the bright mode). Secondly, though the phase shift between two neighboring PIT windows is 2π, it only corresponds to a π phase shift in each ribbon (see Appendix D for more details). Therefore, there are $b+d-1$ transparency windows for PITb-d within one period shift on the condition that $W_1 + W_2 < \Lambda$ (under this condition, each ribbon will strongly couple with only one ribbon in the other layer within each period). These transmission windows open and close with the relative position change and, thus, with the phase difference and the related coupling strength between the ribbons. These intriguing properties are well described and predicted by the PWF (please see Sec. S2 in the Supplemental Material [44] for more details about the discussions on coupling distance and the comparation between the numerical and the theoretical results from PWFs).

To confirm the theoretical model discussed above and verify its generality, we further examine it on the PIT effects that are induced by the $j = 3$ mode and show the corresponding results in Figs. S8–S11 and discuss them in Sec. S6 in the Supplemental Material [44]. These results reveal that the PIT effects appear (disappear) near the positions where the coupling strength obtains its maximum (minimum), and more importantly, the phase difference approaches odd (even) multiple numbers of π.

Therefore, we can answer the questions raised in the introduction. Symmetry breaking is not a general method to achieve all-order PIT because it cannot guarantee a phase difference of odd multiple numbers of π. However, for the common dipole-dipole coupled PIT effect, the breaking of symmetry results in a phase difference near π, leading to the excitation of PIT. That is to say, the existence of the PIT cannot be simply described by the structural symmetry; this is because it fails to capture every detail of the resonant phase, especially for the high-order modes.

In addition to the general rules controlling the existence of the PIT effects, the resonant fields at the two PIT peaks also share a remarkable property. One can find in Figs. 4 and S4 and S8 in the Supplemental Material [44] that the odd-order modes always keep the same resonance field since they are directly excited by the external field, while the even-order modes indicate an in-phase (SM) and out-of-phase (AM) resonance at the peak with a longer and shorter wavelength, respectively. It is indeed the revision of the resonant field of the even-order modes that causes the energy difference of the SM and AM and further gives rise to the existence of the two absorption peaks of the PIT effects.

Remarkably, there are three facts that need emphasizing in this paper so far. The first one is that the underlying physics of the proposed PIT effects are different from the ordinary plasmonic hybridization in paired, coplanar, and stacked arrays of graphene ribbons, where the plasmon interactions are only within ribbons with the same width [55,56] and the energy splittings are due to the bonding and antibonding eigenmode hybridizations of the same order modes in each ribbon [55]. Secondly, since the PIT effects discussed here are achieved by the unidirectional coupling from odd- to even-order mode and, on the other hand, the odd (even)-order mode is assumed to be

excited on the first (second) ribbon layer, the PIT effects are only shown to be induced from the coupling from the first ribbon layer to the second one. However, the physical mechanism allows us to couple from the second ribbon layer to the first layer, depending on the ribbon width, the phase difference, and the order of PIT (see Sec. S3 in the Supplemental Material [44] for more detail). Therefore, our proposal is different with other bidirectional coupling-induced PIT effects [23,57], where the coupling is within the same order modes and is either from the first layer to the second one or on the contrary. Thirdly, though the highest order of the dark mode reaches the 10th (14th) for the cases induced by the first (third) order mode, which is already the highest mode order in the PIT effects, it is expected to be further improved by using a larger period of the ribbon array.

D. Existence of proposed PIT effects

In addition to the above salient features, the proposed mechanism allows realizing the PIT effects with good tolerance to the geometrical imperfections, e.g., the relative ribbon position and the ribbon width. Specifically, as shown in Fig. 4 as well as in Figs. S4, S10, and S11 in the Supplemental Material [44], the PIT window exists and becomes pronounced with two notable absorption peaks almost as long as the phase difference is unequal to odd multiple numbers of π, which means all ordered PIT effects can be induced for a wide range of relative ribbon positions. In addition, it is also interesting to find that a wide range of the second ribbon width can also induce PIT, as shown in Figs. 3(a) and S8(a) in the Supplemental Material [44]. This is because the coupling strength calculated by the PWF remains a notably big value, and at the same time, the phase difference is around odd multiple numbers of π, which guarantee the conditions of allowing the existence of PIT. To make this clearer, we plot the ranges of the ribbon width and the corresponding phase difference in Fig. 5. For example, the PIT1-10 effect maintains a minimum absorption of 5% provided that the width fails within 776–989 nm, which corresponds to a span of 212 nm. Meanwhile, the corresponding phase difference changes from 8.85π to 9.11π, which is around nine times of π. These fantastic properties guarantee the existence of PIT by engineering without stringent geometrical requirements, making it experimentally accessible and giving significant freedom in the design of devices.

E. Sensing performance of PIT effects

Due to the one-atom-thick nature of graphene, graphene plasmons are extremely confined to their surface, making them highly sensitive to the environment [58]. As a result, the induced SM and AM discussed here are extremely sensitive to the local dielectric environment surrounding the two ribbon layers, providing an effective route to design a refractive index sensor. Therefore, it will be interesting to exploit the sensing application of the proposed PIT effects and reveal how the mode order affects the sensing performance. Figure 6 uncovers the sensing properties in the terms of the sensitivity and the corresponding quality factor (Q-factor), which are defined as the plasmon peak shift in the wavelength caused by the change

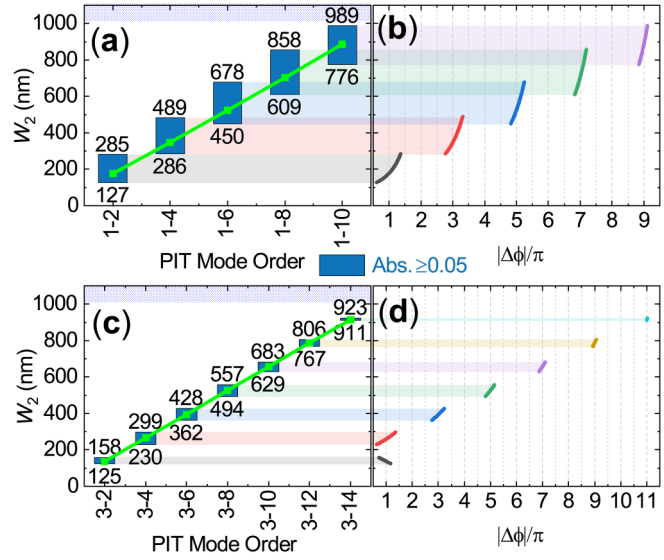

FIG. 5. Ranges of the second layer ribbon width corresponding to the cases with absorption maxima of the two peaks not smaller than 5% for differently ordered plasmonically induced transparency (PIT) effects that are induced by the (a) first-order and (c) third-order modes, respectively. The green square symbols in (a) and (c) correspond to the values shown in Figs. 3(b) and S8(b) in the Supplemental Material [44], respectively, while the green straight lines are the guides for the eye. The upper and lower numbers refer to the maxima and minima values of the width. Phase difference for the corresponding ribbon width in the second ribbon layer for PIT effects induced by the (b) first-order and (d) third-order bright modes, respectively.

of the dielectric medium in one refractive index unit (RIU) and the ratio of the plasmon wavelength to the full width at half-maximum of its peak, respectively. To distinguish the effects of both the bright and dark modes on the sensitivity, we assume that the sensing region can be either above the

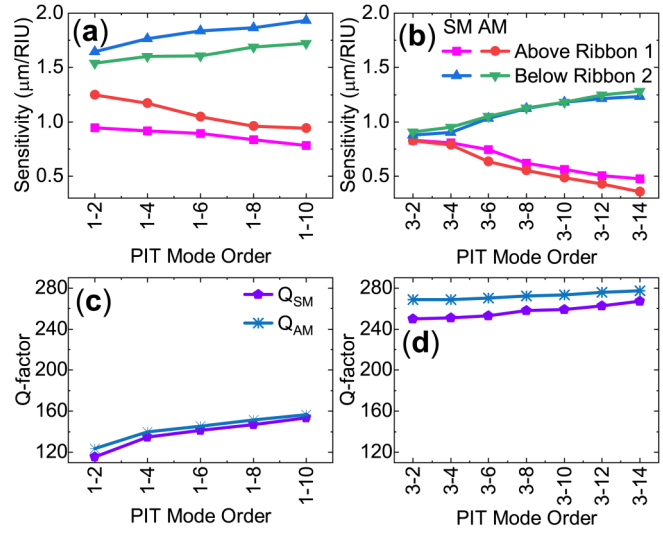

FIG. 6. (a) and (b) Refractive index sensitivities and (c) and (d) Q factors of the proposed plasmonically induced transparency (PIT) effects for different ordered PIT.

first bright mode layer (sensing region n_1) or below the second dark mode layer (sensing region n_3), respectively.

Firstly, it is found that the sensitivity of the case with the sensing region below the second ribbon layer is higher than that of the case with the sensing region above the first ribbon layer for all mode orders, as can be seen in Figs. 6(a) and 6(b), which means the dark mode exhibits a better sensing performance than the bright mode. The reason for this can be figured out by considering two primary effects that directly emerge with the change of mode order. On the one hand, as shown in Figs. 3(b) and S8(b) in the Supplemental Material [44], the absorptions of both the SM and AM decrease with increasing mode order, which means the resonant fields of these modes also reduce with the increase of the mode order. Further considering the known fact that the stronger the resonant field, the bigger the sensitivity [59], we can conclude that the sensitivities tend to reduce with increasing mode order due to the diminishing resonant field. On the other hand, the increase of mode order is accompanied by the increase of the ribbon width of the dark mode resonator, which contributes to an expansion of the dominant sensing region and thus can benefit the sensing performance by boosting the sensitivity. These two aspects indicate that the increasing mode order imposes a tradeoff between the increase and the decrease of sensitivity. Specifically, for the case with the sensing region above the first ribbon layer, only the increasing mode-order-induced degraded resonant field affects it and, therefore, the sensitivity decreases with mode order. Meanwhile, for the case with the sensing region below the second ribbon layer, the two aspects simultaneously play a role, but the effect of the increased sensing region dominates, resulting in the improvement of the sensitivities. Consequently, the sensitivity gap between these two cases continues to widen with increasing mode order.

In addition to the sensitivity, the sensing performance also benefits from the high mode order from the high Q-factor. As can be seen from Figs. 6(c) and 6(d), the Q-factors increase with increasing mode order for all-order PIT. The Q-factors of the PIT modes induced by the third-order bright mode are almost two times those of the PIT effects induced by the first-order bright mode, indicating that the dual-band sensing can benefit from the PIT effects that are induced by high-order bright modes. In general, the proposed high-order PIT effects are expected to be useful for highly sensitive plasmonic sensors that can benefit from high Q-factor resonances.

III. CONCLUSIONS

Different from general ways to achieve PIT by simply breaking the structural symmetry, where only a limited lowest-order PIT effect can be realized, in this paper, we have proposed using a parameter called phase difference to break this limitation and predict the existence of all-order PIT. Owing to its ability to capture the detail of the plasmon resonant phase, this parameter indicates that the PIT effects take place (disappear) generally near the positions where the phase difference is around odd (even) multiple numbers of π. To this end, a model with two layers of stacked GNRs is built to reveal the underlying physics, where multi-order PIT effects up to PIT1-10 and PIT3-14 are achieved to support the governing rules. Additionally, we find that the existence of these PIT effects is guaranteed by the significant freedom in the choice of geometrical parameters while the high-order PIT effects possess blueshifts, high sensitivities, and high Q-factors. Considering that general ways to achieve PIT only depend on breaking structural symmetry while failing to capture the details about the mode order and distribution of the resonant phase, in this paper, we have stepped forward to study the existence of PIT by building up the relationship between the relative position of resonators and the resonant phase distribution of diversely ordered modes through the well-defined phase difference.

Therefore, in this paper, we provide guidance for the design of multistructured PIT devices. For example, it can benefit the design of layered, coplanar, or other nanostructured 2D material-based PIT devices from how to choose the geometrical parameters and set the relative position of the resonators. The findings in this paper provide a fundamental understanding of the existence of PIT and pave the way to the precise designs of on-chip devices that can realize multifunctional applications, such as slowing light, sensing, perfect absorption, and controlling the state of light.

ACKNOWLEDGMENTS

This paper was supported by the National Natural Science Foundation of China (Grants No. 11904096, No. 61775055, No. 61835004, No. 61875133, and No. 11874269), the Natural Science Foundation of Hunan Province, China (Grant No. 2020JJ5028), and the Fundamental Research Funds for the Central Universities.

APPENDIX A: PLASMONIC EIGENMODES AND WAVE FUNCTIONS IN SINGLE GNRs

The PWF has been shown as a powerful and successful tool to describe the electromagnetic field in one-dimensional (1D) and three-dimensional (3D) GNRs and nanodisks [23,39,51,56,58,60–65]. In this paper, following the formalism presented in these works, we further explore and apply it to the situation with a 1D case but two ribbon layers. Considering that the periodic GNRs under study are much smaller than the incident light wavelengths, therefore, we can safely describe their plasmonic response under the electrostatic limit. The nanoribbons are however taken to be large enough to be described as infinitesimally thin domains characterized by a local, homogeneous, and frequency-dependent 2D conductivity $\sigma(\omega)$. Based on the proposed structures shown in Fig. 1(a), we aim to find the electric field $\mathbf{E}$ produced on a planar GNR illuminated by a normal-incidence plane wave of an external field arriving from the y direction $\mathbf{E}^{\text{ext}}(x,\omega) = E^{\text{ext}}\exp[-i\omega(y/c+t)]\cdot\hat{\mathbf{x}}$. The system possesses translational symmetry, so the z component of the electric field is zero. We can formulate a self-consistent equation for the remaining in-plane electric field component in the graphene [23,56,62]:

$$E(x,\omega) = E^{\text{ext}}(x,\omega) + \frac{i}{\varepsilon_{\text{avg}}\omega}\frac{\partial}{\partial x}\int\int \frac{dx'dz}{\sqrt{(x-x')^2+z^2}} \times\left[\frac{\partial}{\partial x'}\sigma(x',\omega)E(x',\omega)\right]. \tag{A1}$$

Here, ε_{avg} is the average permittivity of the two media surrounding the graphene sheet. The expression in square brackets is the induced charge density on the graphene, and the integral calculates the induced scalar potential, which in turn can be written in terms of the current via the continuity equation [51], where we describe graphene by means of a local and homogeneously doped surface conductivity $\sigma(x, \omega)$ and incorporate the dependence on nanoribbon position x by writing $\sigma(x, \omega) = \sigma(\omega) f(x)$, where $f(x)$ is a filling function that is 1 when the in-plane 1D position x lies within the GNR and 0 otherwise. It should be noted that the present formalism of the surface conductivity $\sigma(\omega)$ can be readily applied to a more realistic inhomogeneous doping profile by transferring the space dependence of the carrier concentration to $f(x)$, where $\sigma(\omega)$ can be computed using either Drude or local-Random Phase Approximation (RPA) models. Defining a dimensionless coordinate $\theta = x/W$, where W is the ribbon width, the normalized electric field [56,62,65]

$$E(\theta, \omega) = W\sqrt{f(\theta)}E(\theta, \omega). \tag{A2}$$

Combining these elements, the self-consistent Eq. (A1) can be recast as

$$E(\theta, \omega) = E^{\text{ext}}(\theta, \omega) + \eta(\omega)\int d\theta' M(\theta, \theta')E(\theta', \omega), \tag{A3}$$

where $\eta(\omega) = i\sigma(\omega)/(\omega W \varepsilon)$ is a dimensionless parameter that contains all the physical characteristics of the graphene [51], and

$$M(\theta, \theta') = \sqrt{f(\theta)f(\theta')}\frac{\partial^2}{\partial\theta^2}\frac{1}{\log|\theta - \theta'|}, \tag{A4}$$

which is a real and symmetric linear operator and is invariant within the exchange of its arguments: $M(\theta, \theta') = M(\theta', \theta)$. As a result, it admits a complete set of real eigenvalues $1/\eta_j$ and orthonormalized eigenmodes ε_j for the jth-ordered mode that can be defined through [51,56,62,65]

$$E_j(\theta, \omega) = \eta_j(\omega)\int d\theta' M(\theta, \theta')E(\theta', \omega), \tag{A5}$$

and satisfy the orthogonality condition

$$\int d\theta E_j(\theta)E_{j'}(\theta) = \delta_{jj'}. \tag{A6}$$

Using the eigenmodes shown above, the solution to Eq. (A3) can be written in terms of these eigenmodes as

$$E(\theta, \omega) = \sum_j \frac{\Omega_j}{1 - \eta(\omega)/\eta_j}E_j(\theta), \tag{A7}$$

where Ω_j is the expansion coefficient which is given by

$$\Omega_j = \int d\theta E_j(\theta)E^{\text{ext}}(\theta, \omega). \tag{A8}$$

By using the closure relation, we can get

$$E^{\text{ext}}(\theta, \omega) = \sum_j \Omega_j E_j(\theta), \tag{A9}$$

by which the induced field can be expressed as

$$E^{\text{ind}}(\theta, \omega) = \sum_j \frac{\Omega_j}{\eta_j/\eta(\omega) - 1}E_j(\theta). \tag{A10}$$

Now it is convenient to define the PWFs associated with mode j as

$$\rho_j(\theta) = \frac{\partial}{\partial\theta}\sqrt{f(\theta)}E_j(\theta), \tag{A11}$$

which corresponds to the induced charge density profiles of the confined plasmon eigenmode j.

Based on Eqs. (A5) and (A6), we find that the PWFs satisfy the orthonormality condition:

$$\int d\theta \int d\theta' \frac{\rho_j(\theta)\rho_{j'}(\theta')}{|\theta - \theta'|} = -\frac{\delta_{jj'}}{\eta_j}. \tag{A12}$$

Using the continuity equation along with Eqs. (A3) and (A9) and following a procedure like the derivation of Eq. (A1), we can write the induced charge density ρ^{ind} as

$$\rho^{\text{ind}}(\theta, \omega) = \frac{\varepsilon_{\text{avg}}}{W}\sum_j \frac{\Omega_j}{1/\eta_j - 1/\eta(\omega)}\rho_j(\theta). \tag{A13}$$

Considering that the GNRs are described within the electrostatic limit, the external plane wave acts as a uniform electric field E^{ext}. Upon integration of Eq. (A8) by parts, we find this equation can be rewritten as

$$\Omega_j = -W\zeta_j E^{\text{ext}}(\theta, \omega), \tag{A14}$$

where

$$\zeta_j = \int d\theta \rho_j(\theta)\theta \tag{A15}$$

is the so-called normalized mode moment, which depicts the spatially normalized total polarizability of the ribbon under external incidence and can be used to describe the symmetry of the mode. At this point, we can deduce the induced electric mode moment as

$$P^{\text{ind}}(\omega) = W^2\int d\theta \rho^{\text{ind}}(\theta, \omega)\theta. \tag{A16}$$

Considering that the nanoribbon polarizability per unit length is defined as $\alpha(\omega) = p^{\text{ind}}(\omega)/E^{\text{ext}}$, which can be expressed as the following equation after inserting Eqs. (A13)–(A15) into Eq. (A16):

$$\alpha(\omega) = \varepsilon_{\text{avg}}W^2\sum_j \frac{\zeta_j^2}{1/\eta(\omega) - 1/\eta_j}. \tag{A17}$$

This polarizability allows us to calculate the transmission and extinction cross-section properties of a GNR by using the corresponding PWFs [56,62]. We are interested in the former one, which will be discussed in the following section for the periodic case.

APPENDIX B: COUPLING AMONG LAYERED GNRs

We now discuss the case with two-layered periodic GNRs, as shown in Fig. 1(a). For conceptual demonstration, we index

the nth ribbon in the lth layer (where l only takes 1 or 2) by ln and its width and center position by W_{ln} and x_{ln}, respectively. We also donate the other parameters of the plasmon modes j in the lnth ribbon as the conductivity $\sigma_{ln}(\omega)$, eigenvalue η_{lnj}, eigenmode $\mathcal{E}_{lnj}$, PWF ρ_{lnj}, and mode moment ζ_{lnj}. The corresponding position vector is defined as $\theta = (x - x_{ln})/W_{ln}$, where x_{ln} is the position of the lnth nanoribbon. The average relative permittivity of the lth layer is ε_l. Note that θ is a global variable that runs over the coordinates of all the nanoribbons and is normalized within each of the corresponding ribbon widths. Based on the above definitions, the induced charge density can be expressed as a sum of the contributions from both near and far nanoribbons in a self-consistent equation [56,62]:

$$\rho^{\text{ind}}(\theta, \omega) = \sum_{lnj} a_{lnj}(\omega)\rho_{lnj}(\theta), \tag{B1}$$

where a_{lnj} is the expansion coefficient, which can be expressed as a self-consistent form after adding the field induced by other ribbons $l'n' \neq ln$ to the external field experienced by each island n:

$$a_{lnj}(\omega) = \frac{\varepsilon_l}{W_{ln}} \frac{1}{1/\eta_{lnj} - 1/\eta_{ln}(\omega)} \times \left[\Omega_{lnj} + \sum_{l'n' \neq ln} \sum_{j'} C_{l,n,j\text{-}l',n',j'} a_{l'n'j'}(\omega) \right]. \tag{B2}$$

Here, $\Omega_{lnj} = -W_{ln}\zeta_{lnj}E^{\text{ext}}$, $\eta_{ln}(\omega) = i\sigma_{ln}(\omega)/(\omega W_{ln}\varepsilon_l)$ is defined based upon the conductivity of nanoribbon ln, and

$$C_{l,n,j\text{-}l',n',j'} = \frac{1}{\zeta_l} \int_{ln} d\mathbf{R} \int_{l'n'} d\mathbf{R}' \frac{\rho_{lnj}(\mathbf{R}) \cdot \rho_{l'n'j'}(\mathbf{R}')}{|\mathbf{R} - \mathbf{R}' + d_{lnl'n'}|} \tag{B3}$$

depicts the coupling strength between plasmon modes j and j' that are respectively excited on nanoribbons ln and $l'n'$ and separated by a distance $d_{ln} = x_{ln} - x_{l'n'}$, with the integration over the normalized position $\mathbf{R}$ of each nanoribbon. Note that the coupling strengths shown above have considered both the interlayer and intralayer couplings and the couplings between both the odd- and even-ordered modes. Once solving Eq. (B3), the induced mode moment on ribbon ln can be written as

$$P_{ln} = \sum_j W_{ln}^2 a_{lnj}\zeta_{lnj}. \tag{B4}$$

Then it is convenient to rewrite Eq. (B2) based on the above moments as

$$P_{ln} = \alpha_{ln}(\omega)\left(E^{\text{ext}} + \sum_{l'n' \neq ln} C_{l,n-l',n'} P'_{\text{ln}} \right), \tag{B5}$$

where

$$C_{l,n-l',n'} = -\sum_j \frac{C_{l,n,j-l',n,j'}}{W_{ln}^2 \zeta_{lnj}^2} \tag{B6}$$

describes the coupling between nanoribbons ln and $l'n'$ from all ordered modes, whereas

$$\alpha_{ln}(\omega) = \varepsilon_l W_{ln}^2 \sum_j \frac{\zeta_{lnj}^2}{1/\eta_{ln} - 1/\eta_{lnj}} \tag{B7}$$

is the ribbon polarizability per unit length of the lnth ribbon.

APPENDIX C: COUPLING IN LAYERED PERIODIC GNRs

For the periodic GNR arrays shown in Fig. 1(a), the uniform ribbon width and periodicity will lead to indiscriminate plasmon modes in each layer. Therefore, the total resonant mode moment and the corresponding polarizability should be independent of ribbon index n but linked to the layer orders. Further considering the geometric symmetry and Bloch's theorem of the system, it is found that $P_{ln} = P_l$ and $\alpha_{ln}(\omega) = \alpha_l(\omega)$. Direct insertion of these expressions into Eq. (B5) leads to

$$P_l = \frac{E^{\text{ext}}}{\alpha_l^{-1}(\omega) - C_l}. \tag{C1}$$

Here, $C_l = \sum_{n \neq 0} C_{l,0-l,n'}$ is a lattice sum running over all coplanar ribbon sites, and we have taken $n = 0$ [66,67]. Note that, in the above equations, we have considered the interactions between all ordered modes instead of the case with dipole-dipole modes only [23,56,61,67].

Finally, considering that the incident wavelength is much larger than the nanoribbon period so that all high-order diffracted beams are evanescent, the far-field zero-order transmission (t) and reflection (r) coefficients of the periodic GNR arrays in the lth layer can be expressed as [61,66,67]

$$t_l = \frac{2n_l^+}{n_l^+ + n_l^-} \left[\frac{\varepsilon_l \alpha_l(\omega) - C_l}{\varepsilon_l \alpha_l(\omega) - C_l - iS_l} \right], \tag{C2}$$

$$r_l = t_l - 1. \tag{C3}$$

Here, the superscript $+/-$ represents the effective refractive index of the dielectric layer above/below the lth graphene layer. Also, $S_l = \text{Im}\{C_l\} + 2k^3/3$ accounts for the coupling to propagating light, with k being the wave vector of the incident light [66,67].

At this point, the absorbance A of the layer is found to be

$$A_l = 1 - |r_l|^2 - |t_l|^2 \frac{n_l^-}{n_l^+}. \tag{C4}$$

For the system with periodic two-layer GNRs (as shown in Fig. 1), we can model it as a planar layered system with three subdivided dielectric layers and two graphene interfaces. Since the ultrathin nature of the graphene sheet can be treated as an interface, we use the transfer matrix method to theoretically calculate the light propagation in the layered system [23,68]. The thickness of the dielectric layer sandwiched between the graphene is much smaller than the propagating wavelength; its propagation phase can be safely neglected. Since incident light only comes from the positive y axis and propagates downward in the negative y direction, the transmission T, reflection R, and absorption A of the multilayer system can be described as [23]

$$R = \left| \frac{r_1 + r_2}{1 + r_1 r_2} \right|^2, \tag{C5}$$

$$T = \left| \frac{t_1 t_2}{1 + r_1 r_2} \right|^2, \tag{C6}$$

$$A = 1 - R - T. \tag{C7}$$

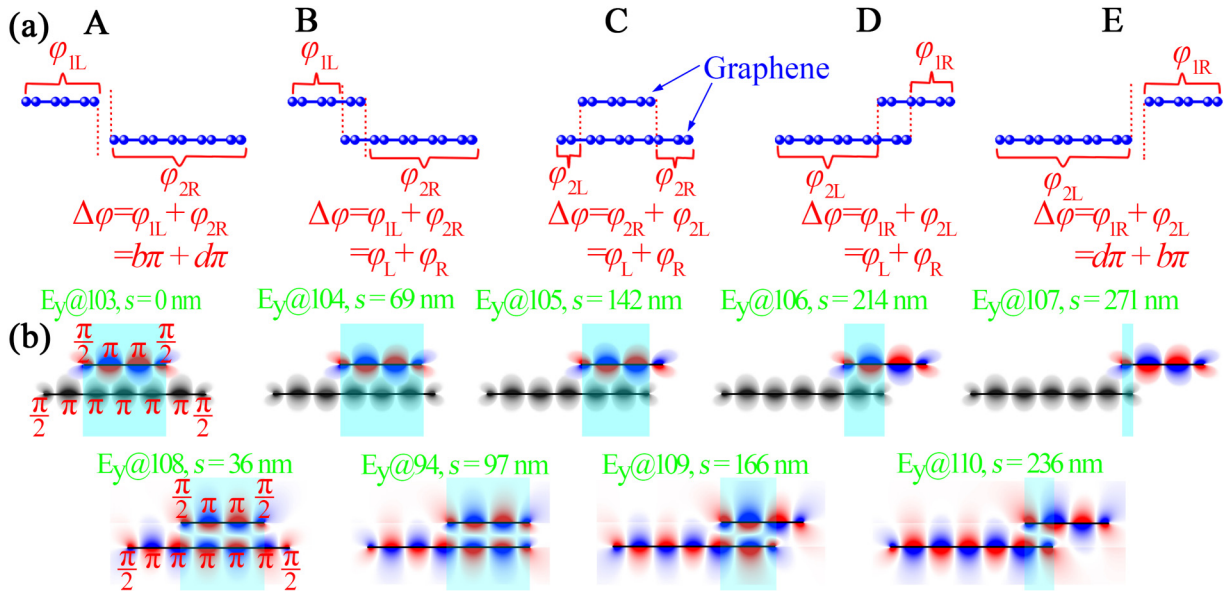

FIG. 7. (a) Schematic diagram of the definitions of the phase difference for five different cases. (b) E_y field distributions of plasmonically induced transparency (PIT)3-6 for different ribbon shifts at the selected positions labeled by the numbers in Fig. S10(g) in the Supplemental Material [44]. Note that the dark-colored fields in the second graphene layer at the positions labeled @103-107 is a guide for the understanding of the phase difference; this is because the sixth mode cannot be excited by the first layer bright mode in the corresponding condition.

APPENDIX D: DEFINITION OF PHASE DIFFERENCE

In this paper, the resonant phase difference $\Delta\varphi$ has been considered a decisive parameter to predicate the existence of the PIT effect. Here, we define it as the difference between the resonant phase of the left/right side of the bright mode to the left/right side of the dark mode. Obviously, this definition has avoided the possible influence of the phase shift at the ribbon edges. Considering that the plasmonic coupling occurs between the y components of the coupled modes, the position-dependent resonant phase in each GNR is calculated by tracking the resonant phase of E_y or the y component of the induced charge density ρ^{ind} [see Eq. (A13)]. Therefore, we can define the resonant phase as

$$\varphi(x) = \arcsin\left(\frac{\rho_y^{\text{ind}}}{|\rho^{\text{ind}}|}\right), \tag{D1}$$

with x being the position within the ribbon area. For the convenience of calculation and discussion, we assume that $\varphi(x)$ monotonically increase from the left to the right part of the ribbon and set the resonant phase and the coordinate at the middle of the dark mode resonator (second ribbon layer, which is assumed to be fixed while the first layer GNR shifts over it) as zero. Based on that, the proposed constructions can be simply classified into five cases for different relative ribbon positions, as shown in Fig. 7(a). By further assuming that $W_1 < W_2$ (the case for $W_1 > W_2$ can be similarly defined by switching the layer order), we can write the phase difference of the five cases as

$$\Delta\varphi = \begin{cases} -b\pi - d\pi, & s \leqslant -\frac{W_1+W_2}{2} \\ \varphi_1\left(s-\frac{W_1}{2}\right) - \varphi_1\left(-\frac{W_2}{2}\right) + \varphi_2\left(s+\frac{W_1}{2}\right) - \varphi_2\left(\frac{W_2}{2}\right), & -\frac{W_1+W_2}{2} < s \leqslant \frac{W_1-W_2}{2} \\ \varphi_2\left(s-\frac{W_1}{2}\right) - \varphi_2\left(-\frac{W_2}{2}\right) + \varphi_2\left(s+\frac{W_1}{2}\right) - \varphi_2\left(\frac{W_2}{2}\right), & \frac{W_1-W_2}{2} < s < -\frac{W_1+W_2}{2} \\ \varphi_2\left(s-\frac{W_1}{2}\right) - \varphi_2\left(-\frac{W_2}{2}\right) + \varphi_1\left(s+\frac{W_1}{2}\right) - \varphi_1\left(\frac{W_2}{2}\right), & -\frac{W_1+W_2}{2} \leqslant s < \frac{W_2+W_1}{2} \\ b\pi + d\pi, & s \geqslant \frac{W_1+W_2}{2} \end{cases} \tag{D2}$$

where the subscripts 1 and 2 refer to the layer order of GNRs, b and d being the mode order of the bright and dark modes, respectively.

Since the phase difference is only related to the relative resonant phase instead of the absolute value of the position (namely, the x coordinate), we can further assume that the absolute values of resonant phases in the two ribbon layers are the same at the ribbon edge of overlapped region. That is, for the case with $W_1 < W_2$ (the case with $W_1 > W_2$ can be obtained likewise) $\varphi_1(-W_2/2) = \varphi_2(-W_2/2)$ for $-(W_1+W_2)/2 < s \leqslant (W_1-W_2)/2$, $\varphi_1(-W_1/2) = \varphi_2(-W_1/2)$ for $(W_1-W_2)/2 < s < (-W_1+W_2)/2$, and $\varphi_1(W_2/2) = \varphi_2(W_2/2)$ for $(-W_1+W_2)/2 \leqslant s < (W_1+W_2)/2$, respectively. Based on this

assumption, we do not need to distinguish the layer order anymore when calculating the phase difference in both the left and right sides. Instead, we extend the resonant phase by connecting the overlapped region since they have same resonant phase at same position. Therefore, we have

$$\Delta\varphi = \begin{cases} b\pi + d\pi, |s| \geqslant \frac{W_1+W_2}{2} \\ \varphi_L+\varphi_R, |s| < \frac{W_1+W_2}{2} \end{cases}, \tag{D3}$$

with $\varphi_L=\varphi(s-W_1/2)-\varphi(-W_2/2)$ and $\varphi_R=\varphi(s+W_1/2)-\varphi(W_2/2)$ are phase difference in the two sides. Therefore, for the five cases labeled A–E, all phase differences can be calculated as the sum of the resonant phases beyond the overlapping region in the left and right sides. Notably, we use the absolute value of phase difference for conceptual discussion throughout our paper.

To show how the phase difference is calculated and make clear the relationship between the PIT effect and the phase difference, we select PIT3-6 as an example, as it is presented in Fig. 7(b). Before going further, we need to note that a sign reverse of the resonant field corresponds to a phase change of π [48,69], while there is about $\pi/2$ phase change and a near-zero phase pickup [70,71] at the edge of the ribbon because the resonant field takes its maximum here. For a standing wave resonance within a ribbon resonator, a plasmon mode with order j will become resonant when it accumulates a $2j\pi$ phase shift for a round trip between the two edges. For the parameters of $W_1 = 200$ nm and $W_2 = 394$ nm, the status of the induced PIT3-6 effects (or correspondingly the sixth-order mode in the second layer) changes from off to on with the relative shift of the first-layer GNR. Specifically, for the cases with $s = 0$, 69, 142, 214, and 271 nm, we get $\varphi_L = 3\pi/2$, $5\pi/2$, $7\pi/2$, $9\pi/2$, and $11\pi/2$ and $\varphi_R = -3\pi/2$, $-\pi/2$, $\pi/2$, $3\pi/2$, and $5\pi/2$, respectively, which means the phase differences are 0, 2π, 4π, 6π, and 8π, respectively. At these conditions, the plasmonic couplings take their minima values (see Fig. S10(h) in the Supplemental Material [44]). As a result, the sixth-order mode cannot be excited by the upper layer bright mode, and therefore, no PIT effect but only one absorption peak is observed in the interested spectral range, as one can see in Fig. S10(g) in the Supplemental Material [44]. However, for the cases with $s = 36$, 97, 166, and 236 nm, one can get $\varphi_L = 2\pi, 3\pi, 4\pi$, and 5π and $\varphi_R = -\pi, 0, \pi$, and 2π, respectively, which means the corresponding phase difference takes 1π, 3π, 5π, and 7π, respectively. In these cases, the plasmonic coupling strength is around their maximum (see Fig. S10(h) in the Supplemental Material [44]), which means the upper layer bright mode couples strongly with the lower high-order dark mode and further leads to distinct PIT effects (see Fig. S10(i) in the Supplemental Material [44]). At this point, the relationship between the phase difference and the existence of the PIT effect stated in the main text has been made clear.

Additionally, one may find that, when the upper ribbon shifts partially beyond the region over the lower ribbon, e.g., cases B and D, the induced PIT peaks are not as high as those corresponding to case C, as is clearly shown in Figs. S10(a), S10(d), S10(g), S10(j), S11(a), S11(d) and S11(g) in the Supplemental Material [44]. This is because the coupling strength becomes weak under this condition, which is clearly shown by the blue line in Figs. S10(b), S10(e), S10(h), S10(k), S11(b), S11(e) and S11(h) in the Supplemental Material [44]. Note that this phenomenon is different from the case with PIT induced by the first-order bright mode when it is compared with those shown in Figs. 4(a), 4(d), 4(g), and S4(a) and S4(d) in the Supplemental Material [44]. However, the PIT effect does not exist for all-order modes when the upper ribbon shifts totally beyond the region over the lower ribbon, as shown in cases A and E; even the phase differences are odd multiple numbers of π (that is, 5π, 7π, 9π, 11π, 13π, and 15π for PIT3-2, PIT3-4, PIT3-6, PIT3-8, PIT3-10, and PIT3-12, respectively, as it is respectively shown in Figs. S10(c), S10(f), S10(i), S10(l), S11(c), and S11(f) in the Supplemental Material [44]). This is because the coupling between the two ribbons approaches zero in these cases, as can be seen in Figs. S10(b), S10(e), S10(h), S10(k), S11(b), and S11(e) in the Supplemental Material [44]. The same phenomenon can also be found in the PIT effects induced by the first-order bright mode.

[1] D. K. Gramotnev and S. I. Bozhevolnyi, Plasmonics beyond the diffraction limit, Nat. Photonics **4**, 83 (2010).

[2] W. L. Barnes, A. Dereux, and T. W. Ebbesen, Surface plasmon subwavelength optics, Nature (London) **424**, 824 (2003).

[3] S. Chakraborty, O. P. Marshall, T. G. Folland, Y. J. Kim, A. N. Grigorenko, and K. S. Novoselov, Gain modulation by graphene plasmons in aperiodic lattice lasers, Science **351**, 246 (2016).

[4] E. Kazuma, J. Jung, H. Ueba, M. Trenary, and Y. Kim, Real-space and real-time observation of a plasmon-induced chemical reaction of a single molecule, Science **360**, 521 (2018).

[5] H. Xin, B. Namgung, and L. P. Lee, Nanoplasmonic optical antennas for life sciences and medicine, Nat. Rev. Mater. **3**, 228 (2018).

[6] L. Duempelmann, A. Luu-Dinh, B. Gallinet, and L. Novotny, Four-fold color filter based on plasmonic phase retarder, ACS Photonics **3**, 190 (2016).

[7] S. I. Azzam, A. V. Kildishev, R.-M. Ma, C.-Z. Ning, R. Oulton, V. M. Shalaev, M. I. Stockman, J.-L. Xu, and X. Zhang, Ten years of spasers and plasmonic nanolasers, Light-Sci. Appl. **9**, 90 (2020).

[8] J. N. Anker, W. P. Hall, O. Lyandres, N. C. Shah, J. Zhao, and R. P. Van Duyne, Biosensing with plasmonic nanosensors, Nat. Mater. **7**, 442 (2008).

[9] Z. Li, Z. Yi, T. Liu, L. Liu, X. Chen, F. Zheng, J. Zhang, H. Li, P. Wu, and P. Yan, Three-band perfect absorber with high refractive index sensing based on an active tunable Dirac semimetal, Phys. Chem. Chem. Phys. **23**, 17374 (2021).

[10] Y. Ren, Q. Chen, M. He, X. Zhang, H. Qi, and Y. Yan, Plasmonic optical tweezers for particle manipulation: principles, methods, and applications, ACS Nano **15**, 6105 (2021).

[11] Y. Zhang, C. Min, X. Dou, X. Wang, H. P. Urbach, M. G. Somekh, and X. Yuan, Plasmonic tweezers: for nanoscale optical trapping and beyond, Light-Sci. Appl. **10**, 59 (2021).

[12] S. Zhang, D. A. Genov, Y. Wang, M. Liu, and X. Zhang, Plasmon-Induced Transparency in Metamaterials, Phys. Rev. Lett. **101**, 047401 (2008).

[13] N. Liu, L. Langguth, T. Weiss, J. Kästel, M. Fleischhauer, T. Pfau, and H. Giessen, Plasmonic analogue of electromagnetically induced transparency at the Drude damping limit, Nat. Mater. **8**, 758 (2009).

[14] J. Chen, Z. Li, S. Yue, J. Xiao, and Q. Gong, Plasmon-induced transparency in asymmetric T-shape single slit, Nano Lett. **12**, 2494 (2012).

[15] R. D. Kekatpure, E. S. Barnard, W. Cai, and M. L. Brongersma, Phase-Coupled Plasmon-Induced Transparency, Phys. Rev. Lett. **104**, 243902 (2010).

[16] B. Peng, Ş. K. Özdemir, W. Chen, F. Nori, and L. Yang, What is and what is not electromagnetically induced transparency in whispering-gallery microcavities, Nat. Commun. **5**, 5082 (2014).

[17] C. Wang, X. Jiang, W. R. Sweeney, C. W. Hsu, Y. Liu, G. Zhao, B. Peng, M. Zhang, L. Jiang, A. D. Stone, and L. Yang, Induced transparency by interference or polarization, Proc. Natl. Acad. Sci. USA **118**, e2012982118 (2021).

[18] M.-W. Chu, V. Myroshnychenko, C. H. Chen, J.-P. Deng, C.-Y. Mou, and F. J. García de Abajo, Probing bright and dark surface-plasmon modes in individual and coupled noble metal nanoparticles using an electron beam, Nano Lett. **9**, 399 (2009).

[19] M. Abb, Y. Wang, P. Albella, C. H. de Groot, J. Aizpurua, and O. L. Muskens, Interference, coupling, and nonlinear control of high-order modes in single asymmetric nanoantennas, ACS Nano **6**, 6462 (2012).

[20] H. Yan, T. Low, F. Guinea, F. Xia, and P. Avouris, Tunable phonon-induced transparency in bilayer graphene nanoribbons, Nano Lett. **14**, 4581 (2014).

[21] A. Artar, A. A. Yanik, and H. Altug, Multispectral plasmon induced transparency in coupled meta-atoms, Nano Lett. **11**, 1685 (2011).

[22] A. B. Yankovich, R. Verre, E. Olsén, A. E. O. Persson, V. Trinh, G. Dovner, M. Käll, and E. Olsson, Multidimensional hybridization of dark surface plasmons, ACS Nano **11**, 4265 (2017).

[23] S. X. Xia, X. Zhai, L. L. Wang, and S. C. Wen, Plasmonically induced transparency in double-layered graphene nanoribbons, Photon. Res. **6**, 692 (2018).

[24] Z. Chai, X. Hu, H. Yang, and Q. Gong, All-optical tunable on-chip plasmon-induced transparency based on two surface-plasmon-polaritons absorption, Appl. Phys. Lett. **108**, 151104 (2016).

[25] T. T. Kim, H. D. Kim, R. Zhao, S. S. Oh, T. Ha, D. S. Chung, Y. H. Lee, B. Min, and S. Zhang, Electrically tunable slow light using graphene metamaterials, ACS Photonics **5**, 1800 (2018).

[26] C. Hu, S. A. Schulz, A. A. Liles, and L. O'Faolain, Tunable optical buffer through an analogue to electromagnetically induced transparency in coupled photonic crystal cavities, ACS Photonics **5**, 1827 (2018).

[27] M. F. Limonov, M. V. Rybin, A. N. Poddubny, and Y. S. Kivshar, Fano resonances in photonics, Nat. Photonics **11**, 543 (2017).

[28] D. B. Litt, M. R. Jones, M. Hentschel, Y. Wang, S. Yang, H. D. Ha, X. Zhang, and A. P. Alivisatos, Hybrid lithographic and DNA-directed assembly of a configurable plasmonic metamaterial that exhibits electromagnetically induced transparency, Nano Lett. **18**, 859 (2018).

[29] N. Liu, T. Weiss, M. Mesch, L. Langguth, U. Eigenthaler, M. Hirscher, C. Sönnichsen, and H. Giessen, Planar metamaterial analogue of electromagnetically induced transparency for plasmonic sensing, Nano Lett. **10**, 1103 (2010).

[30] Y. Hu, T. Jiang, H. Sun, M. Tong, J. You, X. Zheng, Z. Xu, and X. Cheng, Ultrafast frequency shift of electromagnetically induced transparency in terahertz metaphotonic devices, Laser Photonics Rev. **14**, 1900338 (2020).

[31] X. Zhao, L. Zhu, C. Yuan, and J. Yao, Tunable plasmon-induced transparency in a grating-coupled double-layer graphene hybrid system at far-infrared frequencies, Opt. Lett. **41**, 5470 (2016).

[32] H. Jung, H. Jo, W. Lee, B. Kim, H. Choi, M. S. Kang, and H. Lee, Electrical control of electromagnetically induced transparency by terahertz metamaterial funneling, Adv. Opt. Mater. **7**, 1801205 (2019).

[33] S. Xiao, T. Wang, T. Liu, X. Yan, Z. Li, and C. Xu, Active modulation of electromagnetically induced transparency analogue in terahertz hybrid metal-graphene metamaterials, Carbon **126**, 271 (2018).

[34] H. Cheng, S. Chen, P. Yu, X. Duan, B. Xie, and J. Tian, Dynamically tunable plasmonically induced transparency in periodically patterned graphene nanostrips, Appl. Phys. Lett. **103**, 203112 (2013).

[35] Z.-J. Yang, Z.-S. Zhang, L.-H. Zhang, Q.-Q. Li, Z.-H. Hao, and Q.-Q. Wang, Fano resonances in dipole-quadrupole plasmon coupling nanorod dimers, Opt. Lett. **36**, 1542 (2011).

[36] Z.-J. Yang, Z.-H. Hao, H.-Q. Lin, and Q.-Q. Wang, Plasmonic Fano resonances in metallic nanorod complexes, Nanoscale **6**, 4985 (2014).

[37] W. Khunsin, J. Dorfmüller, M. Esslinger, R. Vogelgesang, C. Rockstuhl, C. Etrich, and K. Kern, Quantitative and direct near-field analysis of plasmonic-induced transparency and the observation of a plasmonic breathing mode, ACS Nano **10**, 2214 (2016).

[38] S. Kim, M. S. Jang, V. W. Brar, K. W. Mauser, L. Kim, and H. A. Atwater, Electronically tunable perfect absorption in graphene, Nano Lett. **18**, 971 (2018).

[39] Z. Fang, S. Thongrattanasiri, A. Schlather, Z. Liu, L. Ma, Y. Wang, P. M. Ajayan, P. Nordlander, N. J. Halas, and F. J. García de Abajo, Gated tunability and hybridization of localized plasmons in nanostructured graphene, ACS Nano **7**, 2388 (2013).

[40] P. A. Huidobro, M. Kraft, S. A. Maier, and J. B. Pendry, Graphene as a tunable anisotropic or isotropic plasmonic metasurface, ACS Nano **10**, 5499 (2016).

[41] P. Kang, K.-H. Kim, H.-G. Park, and S. Nam, Mechanically reconfigurable architectured graphene for tunable plasmonic resonances, Light-Sci. Appl. **7**, 17 (2018).

[42] J. Nong, L. Tang, G. Lan, P. Luo, Z. Li, D. Huang, J. Yi, H. Shi, and W. Wei, Enhanced graphene plasmonic mode energy for highly sensitive molecular fingerprint retrieval, Laser Photonics Rev. **15**, 2000300 (2021).

[43] G. W. Hanson, Dyadic Green's functions and guided surface waves for a surface conductivity model of graphene, J. Appl. Phys. **103**, 064302 (2008).

[44] See Supplemental Material at http://link.aps.org/supplemental/10.1103/PhysRevB.106.075401 for details about Sec. S1: The conductivity model of the graphene; Sec. S2: Model of FDTD calculations; Sec. S3: Absorption maps with different GNR

layers; Sec. S4: High-order PIT effects induced by the first-order odd mode; Sec. S5: Discussion on the blue shift of the high-order PIT; Sec. S6: High-order PIT effects induced by the third-order odd mode; and Sec. S7: Comparison of the first-five-order nearest-neighbor coupling strength. References [72–79] are included there.

[45] W. Tang, L. Wang, X. Chen, C. Liu, A. Yu, and W. Lu, Dynamic metamaterial based on the graphene split ring high-Q Fano-resonnator for sensing applications, Nanoscale **8**, 15196 (2016).

[46] C.-F. Chen, C.-H. Park, B. W. Boudouris, J. Horng, B. Geng, C. Girit, A. Zettl, M. F. Crommie, R. A. Segalman, S. G. Louie, and F. Wang, Controlling inelastic light scattering quantum pathways in graphene, Nature (London) **471**, 617 (2011).

[47] A. Y. Nikitin, P. Alonso-González, S. Vélez, S. Mastel, A. Centeno, A. Pesquera, A. Zurutuza, F. Casanova, L. E. Hueso, F. H. L. Koppens, and R. Hillenbrand, Real-space mapping of tailored sheet and edge plasmons in graphene nanoresonators, Nat. Photonics **10**, 239 (2016).

[48] K. A. Velizhanin, Geometric universality of plasmon modes in graphene nanoribbon arrays, Phys. Rev. B **91**, 125429 (2015).

[49] A. Y. Nikitin, T. Low, and L. Martin-Moreno, Anomalous reflection phase of graphene plasmons and its influence on resonators, Phys. Rev. B **90**, 041407(R) (2014).

[50] K. O. Wedel, N. A. Mortensen, K. S. Thygesen, and M. Wubs, Edge-dependent reflection and inherited fine structure of higher-order plasmons in graphene nanoribbons, Phys. Rev. B **99**, 045411 (2019).

[51] F. J. Garcıía de Abajo, Multiple excitation of confined graphene plasmons by single free electrons, ACS Nano **7**, 11409 (2013).

[52] X. Xiao, X. Li, J. D. Caldwell, S. A. Maier, and V. Giannini, Theoretical analysis of graphene plasmon cavities, Appl. Mater. Today **12**, 283 (2018).

[53] L. Ju, B. Geng, J. Horng, C. Girit, M. Martin, Z. Hao, H. A. Bechtel, X. Liang, A. Zettl, Y. R. Shen, and F. Wang, Graphene plasmonics for tunable terahertz metamaterials, Nat. Nanotechnol. **6**, 630 (2011).

[54] S. X. Xia, X. Zhai, L. L. Wang, B. Sun, J. Q. Liu, and S. C. Wen, Dynamically tunable plasmonically induced transparency in sinusoidally curved and planar graphene layers, Opt. Express **24**, 17886 (2016).

[55] J. Christensen, A. Manjavacas, S. Thongrattanasiri, F. H. L. Koppens, and F. J. García de Abajo, Graphene plasmon waveguiding and hybridization in individual and paired nanoribbons, ACS Nano **6**, 431 (2012).

[56] I. Silveiro, J. M. P. Ortega, and F. J. G. d. Abajo, Plasmon wave function of graphene nanoribbons, New J. Phys. **17**, 083013 (2015).

[57] J. Guan, S. Xia, Z. Zhang, J. Wu, H. Meng, J. Yue, X. Zhai, L. Wang, and S. Wen, Two switchable plasmonically induced transparency effects in a system with distinct graphene resonators, Nanoscale Res. Lett. **15**, 142 (2020).

[58] D. Rodrigo, O. Limaj, D. Janner, D. Etezadi, F. J. García de Abajo, V. Pruneri, and H. Altug, Mid-infrared plasmonic biosensing with graphene, Science **349**, 165 (2015).

[59] S. Xia, X. Zhai, Y. Huang, J. Liu, L. Wang, and S. Wen, Graphene surface plasmons with dielectric metasurfaces, J. Lightwave Technol. **35**, 4553 (2017).

[60] F. J. García de Abajo and A. Manjavacas, Plasmonics in atomically thin materials, Farad. Discuss. **178**, 87 (2015).

[61] F. J. García de Abajo, Graphene plasmonics: challenges and opportunities, ACS Photonics **1**, 135 (2014).

[62] R. Yu, J. D. Cox, J. R. M. Saavedra, and F. J. García de Abajo, Analytical modeling of graphene plasmons, ACS Photonics **4**, 3106 (2017).

[63] S. Sanders, A. May, A. Alabastri, and A. Manjavacas, Extraordinary enhancement of quadrupolar transitions using nanostructured graphene, ACS Photonics **5**, 3282 (2018).

[64] I. Alonso Calafell, J. D. Cox, M. Radonjić, J. R. M. Saavedra, F. J. García de Abajo, L. A. Rozema, and P. Walther, Quantum computing with graphene plasmons, npj Quantum Inform. **5**, 37 (2019).

[65] V. Mkhitaryan, E. J. C. Dias, F. Carbone, and F. J. García de Abajo, Ultrafast momentum-resolved free-electron probing of optically pumped plasmon thermal dynamics, ACS Photonics **8**, 614 (2021).

[66] F. J. García de Abajo, Colloquium: Light scattering by particle and hole arrays, Rev. Mod. Phys. **79**, 1267 (2007).

[67] S. Thongrattanasiri, F. H. L. Koppens, and F. J. García de Abajo, Complete Optical Absorption in Periodically Patterned Graphene, Phys. Rev. Lett. **108**, 047401 (2012).

[68] H. Lu, X. Gan, B. Jia, D. Mao, and J. Zhao, Tunable high-efficiency light absorption of monolayer graphene via Tamm plasmon polaritons, Opt. Lett. **41**, 4743 (2016).

[69] S. X. Xia, X. Zhai, L. L. Wang, Q. Lin, and S. C. Wen, Excitation of crest and trough surface plasmon modes in in-plane bended graphene nanoribbons, Opt. Express **24**, 427 (2016).

[70] J. Chen, M. Badioli, P. Alonso-González, S. Thongrattanasiri, F. Huth, J. Osmond, M. Spasenović, A. Centeno, A. Pesquera, P. Godignon *et al.*, Optical nano-imaging of gate-tunable graphene plasmons, Nature (London) **487**, 77 (2012).

[71] S. X. Xia, X. Zhai, Y. Huang, J. Q. Liu, L. L. Wang, and S. C. Wen, Multi-band perfect plasmonic absorptions using rectangular graphene gratings, Opt. Lett. **42**, 3052 (2017).

[72] A. N. Grigorenko, M. Polini, and K. S. Novoselov, Graphene plasmonics, Nat. Photonics **6**, 749 (2012).

[73] Q. Bao, H. Zhang, B. Wang, Z. Ni, C. H. Y. X. Lim, Y. Wang, D. Y. Tang, and K. P. Loh, Broadband graphene polarizer, Nat. Photonics **5**, 411 (2011).

[74] W. Gao, J. Shu, C. Qiu, and Q. Xu, Excitation of plasmonic waves in graphene by guided-mode resonances, ACS Nano **6**, 7806 (2012).

[75] F. H. L. Koppens, D. E. Chang, and F. J. García de Abajo, Graphene plasmonics: a platform for strong light–matter interactions, Nano Lett. **11**, 3370 (2011).

[76] B. Wang, X. Zhang, X. Yuan, and J. Teng, Optical coupling of surface plasmons between graphene sheets, Appl. Phys. Lett. **100**, 131111 (2012).

[77] Z. Fang, Y. Wang, A. E. Schlather, Z. Liu, P. M. Ajayan, F. J. García de Abajo, P. Nordlander, X. Zhu, and N. J. Halas, Active tunable absorption enhancement with graphene nanodisk arrays, Nano Lett. **14**, 299 (2014).

[78] V. W. Brar, M. S. Jang, M. Sherrott, J. J. Lopez, and H. A. Atwater, Highly confined tunable mid-infrared plasmonics in graphene nanoresonators, Nano Lett. **13**, 2541 (2013).

[79] D. Rodrigo, A. Tittl, O. Limaj, F. J. G. d. Abajo, V. Pruneri, and H. Altug, Double-Layer graphene for enhanced tunable infrared plasmonics, Light-Sci. Appl. **6**, e16277 (2017).